

In Situ Electrochemical ESR and Voltammetric Studies on the Anodic Oxidation of *para*-Haloanilines in Acetonitrile

Ian Streeter, Andrew J. Wain, Mary Thompson, and Richard G. Compton*

Physical and Theoretical Chemistry Laboratory, Oxford University, South Parks Road,
Oxford OX1 3QZ, United Kingdom

Received: February 23, 2005; In Final Form: April 11, 2005

An in situ electrochemical electron spin resonance (ESR) study on the electro-oxidation of *para*-chloroaniline, *para*-bromoaniline, and *para*-iodoaniline dissolved in acetonitrile at gold electrodes is reported. ESR spectra obtained using a tubular flow cell reveal the presence of a paramagnetic dimer product derived from *para*-aminodiphenylamine, during oxidative electrolysis, suggesting the coupling of reactive electrogenerated radical cations with neutral parent haloaniline molecules. The ESR signal intensity behaves in a manner expected for a radical species reacting with second-order kinetics, suggesting the paramagnetic dimer is, itself, unstable. The theory describing the ESR signal intensity flow rate behavior for this reaction mechanism is developed for the tubular arrangement and used to extract mechanistic and kinetic data from the experimental results for the cases of *para*-chloroaniline and *para*-bromoaniline. Further mechanistic aspects, including proton and halide ion expulsion during dimerization, are explored voltammetrically and with the aid of digital simulations using Digisim. Comparison of the ESR signal and voltammetric measurements suggests that an additional mechanism operates which does not lead to paramagnetic products. Additionally, the in situ electrolysis of *N,N*-dimethyl-*para*-bromoaniline is reported to generate the stable radical cation of *N,N,N',N'*-tetramethylbenzidine, and a mechanism of electro-oxidation is, thus, proposed.

1. Introduction

There is a vast array of literature surrounding the electrochemical oxidation of aniline in a variety of solvents, much of which stems from the fact that this process is known to yield polyaniline, a very commonly studied and commercially important conducting polymer, with applications in a range of technological fields, such as the development of rechargeable batteries, electronic and electrochromic devices, and pH sensor design.^{1–8} The complexity of the anodic oxidation of aniline has provoked a number of investigations in which a range of substituents occupy various positions of the aromatic ring in order to probe mechanistic aspects of the electro-dimerization and ultimately the polymerization which takes place.^{9–13}

In a recent collection of papers, Farsang and co-workers^{14–19} studied the electrochemical oxidation of *para*-haloanilines in DMF¹⁴ and acetonitrile,^{15–19} developing earlier work by Adams and Bacon in aqueous media.¹³ In all cases, the anodic oxidation was reported to proceed via a single electron transfer to generate the corresponding radical cation, which was found to undergo further chemical reaction to ultimately form an electrogenerated dimer product. It was concluded from fast scan voltammetry that, in DMF, the mechanism proceeds via fast deprotonation of the primary radical cation to form a neutral radical which couples with the parent radical cation with the formation of a nitrogen–carbon bond, the final product forming via ejection of the corresponding hydrogen halide (see Scheme 1).¹⁴

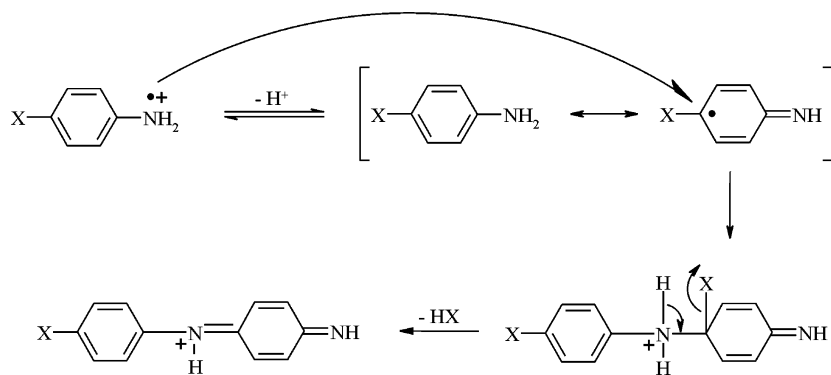
Electrochemical electron spin resonance (ESR) has been used to study a multitude of cases in which electrochemically

generated radical species undergo dimerization reactions, and much information can be gained as to the kinetics and mechanism of such electro-dimerization processes.^{20–24} In this paper, we report the detection of a paramagnetic species formed during the in situ electrochemical oxidation of three *para*-haloanilines using a tubular flow cell, in which the recorded spectrum appears to resemble that of the radical cation of *para*-aminodiphenylamine. A mechanism is proposed which is thought to occur in parallel to that in Scheme 1, where the haloaniline is oxidized to the corresponding radical cation, which, after deprotonation, reacts with a parent haloaniline molecule to yield a dimer radical cation which, although visible on the ESR experimental time scale, is shown to undergo bimolecular decay, resulting in a weak ESR signal. The theory describing the tubular cell ESR signal flow rate behavior for the postulated mechanism is developed, and kinetic parameters for the proposed mechanism are estimated by simulation of the experimental data for the cases of *para*-chloroaniline and *para*-bromoaniline. The dimerization step of the proposed parallel route is found to take place slowly on the voltammetric time scale, causing an inconsistency in the kinetic parameters extracted from the limiting current data (which probes the *electrode surface*) and the ESR signal *downstream* from the electrode, which is in support of this dual mechanism.

Mechanistic details, such as the ejection of protons and halide ions during the course of dimerization, are investigated using cyclic voltammetry and Digisim modeling. The electrochemical oxidation of an *N*-methylated haloaniline analogue, *N,N*-dimethyl-*para*-bromoaniline, is also reported to proceed with the generation of a stable paramagnetic dimer, which is identified as the radical cation of *N,N,N',N'*-tetramethylbenzidine.

* To whom all correspondence should be addressed. E-mail: richard.compton@chemistry.oxford.ac.uk. Phone: +44 (0) 1865 275 413. Fax: +44 (0) 1865 275 410.

SCHEME 1



2. Theory

2.1. Tubular Electrode Model. The full mass transport equation for laminar flow in a tube of constant radius is

$$\frac{\partial c}{\partial t} = D \left(\frac{\partial^2 c}{\partial r^2} + \frac{1}{r} \frac{\partial c}{\partial r} + \frac{\partial^2 c}{\partial x^2} \right) - v_x \frac{\partial c}{\partial x} \quad (1)$$

as described in previous work,^{25–30} where c is the concentration of the electroactive species, D is its diffusion coefficient, and v_x is the flow rate as defined by the parabolic equation³¹

$$v_x = v_0 \left(1 - \frac{r^2}{\rho^2} \right) \quad (2)$$

in which v_0 is the maximum flow velocity, at the tube center (Figure 1). The terms in eq 1 represent diffusion in the radial direction and diffusion and convection in the axial direction. It has been shown that for all but the slowest of flow rates corresponding to Peclet numbers, Pe , of less than $\log Pe \approx 2$, where $Pe = (4V_{Fe}^2)/(\pi D_A \rho^3)$, axial diffusion may be neglected due to the much greater importance of the convection term;^{32,33} throughout this work, the flow rates used are fast enough that this term may legitimately be ignored.

Previous models^{28–30,34} have used the L  v  que approximation,^{31,32} which assumes the flow profile to be linear rather than taking into account its parabolic nature, meaning that the approximation only holds when the diffusion layer thickness is much smaller than the radius of the tube. In this case, the distance of the diffusion layer from the tube center, r , is approximately equal to the tube radius, ρ , leading to the approximation $v_x \approx (2\nu_0 y/\rho)$.

However, it has been shown that for Peclet numbers lower than $\log Pe \approx 6$ the parabolic flow profile is important over the area of the electrode.³² Since in this work it is necessary to simulate a length of tube much longer than the electrode length, even for thin diffusion layers over the electrode, it is likely that over the whole length of the tube the linear approximation will not be valid. Therefore, the equation used in our model neglects the axial diffusion term but takes into account the full parabolic flow profile:

$$\frac{\partial c}{\partial t} = D \left(\frac{\partial^2 c}{\partial r^2} + \frac{1}{r} \frac{\partial c}{\partial r} \right) - v_0 \left(1 - \frac{r^2}{\rho^2} \right) \frac{\partial c}{\partial x} = 0 \quad (3)$$

The experimental measurements reported below are performed under limiting current conditions; hence, in the calculations, it is only the steady state solution that is evaluated and $\partial c/\partial t$ is set to 0.

The Levich solution for the limiting current in a tubular cell linearizes the flow profile using the L  v  que approximation and neglects the radial diffusion term, so that the equation used is analogous to that for a channel flow cell. This gives rise to the Levich expression for the limiting current at a tube electrode:^{30–32}

$$i_{\text{lim}} = 5.24 \times 10^5 n F A_{\text{bulk}} x_e^{2/3} D_A^{2/3} V_f^{1/3} \quad (4)$$

2.2. ESR Signal. The ESR sensitivity shows a $\sin^2 x$ dependence over the length of the cavity, so to evaluate the ESR signal, this profile convolutes the number of spins distributed in the cavity.²⁶ Thus, over the sensitive length of the tube, as shown in Figure 1, the ESR signal is given by

$$\text{signal} = S_0 \int_{x_u + x_{\text{gap}} + x_e}^{x_d} \sin^2\left(\frac{x - x_u}{l} \pi\right) \int_0^\rho 2\pi r c(r, x) \, dr \, dx \quad (5)$$

where x_u and x_d are the upstream and downstream ends of the sensitive cavity, as shown in Figure 1, and l is a characteristic length, which in this case is equal to the cavity length.

2.3. Homogeneous Kinetics. In section 4.2, experimental observations lead to the proposed reaction mechanism given in Scheme 2, and in section 4.3, further mechanistic aspects are discussed. For the purposes of simulation, this mechanism can

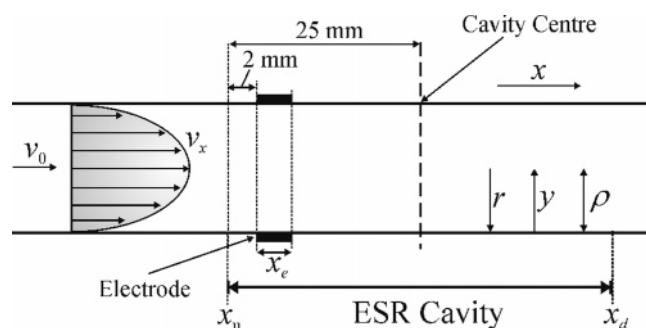
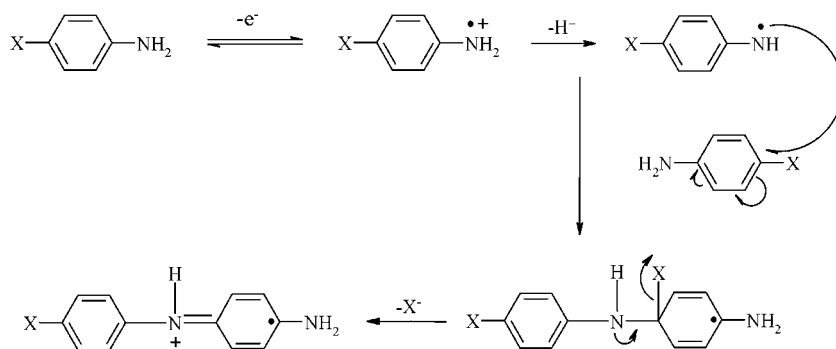


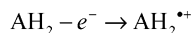
Figure 1. Diagram of the tubular flow cell and the parabolic flow profile.

SCHEME 2

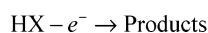
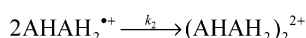
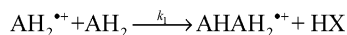


SCHEME 3

Electrode:



Homogeneous reactions:



be simplified to that shown in Scheme 3, where AH_2 is the original haloaniline, $\text{AH}_2^{\bullet+}$ is the oxidized form, and $\text{AHAH}_2^{\bullet+}$ is the adduct formed from AH_2 and $\text{AH}_2^{\bullet+}$ after the loss of hydrogen halide, HX , which itself undergoes a one electron oxidation at the electrode. The adduct $\text{AHAH}_2^{\bullet+}$ is then thought to dimerize, thus undergoing a second-order decay.

Then, the dimensionless partial differential equations^{26,28,32} describing the above species are composed of the convective diffusion equation plus terms describing the homogeneous kinetics (in order to simplify the algebra, the following notation has been employed: $A = \text{AH}_2$, $B = \text{AH}_2^{\bullet+}$, $C = \text{AHAH}_2^{\bullet+}$, and $E = \text{HX}$)

$$\frac{\partial a}{\partial T} = \frac{\partial^2 a}{\partial Y^2} + \frac{1}{p-Y} \frac{\partial a}{\partial Y} - \frac{PeY(2p-Y)}{2p} \frac{\partial a}{\partial X} - K_1 ab = 0 \quad (6)$$

$$\frac{\partial b}{\partial T} = \frac{D_B}{D_A} \left(\frac{\partial^2 b}{\partial Y^2} + \frac{1}{(p-Y)} \frac{\partial b}{\partial Y} \right) - \frac{PeY(2p-Y)}{2p} \frac{\partial b}{\partial X} - K_1 ab = 0 \quad (7)$$

$$\frac{\partial c}{\partial T} = \frac{D_C}{D_A} \left(\frac{\partial^2 c}{\partial Y^2} + \frac{1}{(p-Y)} \frac{\partial c}{\partial Y} \right) - \frac{PeY(2p-Y)}{2p} \frac{\partial c}{\partial X} + K_1 ab - K_2 c^2 = 0 \quad (8)$$

$$\frac{\partial e}{\partial T} = \frac{D_E}{D_A} \left(\frac{\partial^2 e}{\partial Y^2} + \frac{1}{(p-Y)} \frac{\partial e}{\partial Y} \right) - \frac{PeY(2p-Y)}{2p} \frac{\partial e}{\partial X} + K_1 ab = 0$$

where $Pe = 4V_{Fe}^2/\pi D_A \rho^3$, $K_1 = k_1 x_e^2 A_{\text{bulk}}/D_A$ and $K_2 = k_2 x_e^2 A_{\text{bulk}}/D_A$, a , b , c , and e are the concentrations of the respective species normalized with respect to A_{bulk} , and T is the normalized time, $T = Dt/x_e^2$. It is clear from these equations that, while the values of k_1 and k_2 (Scheme 3) will both affect the ESR signal due to $\text{AHAH}_2^{\bullet+}$ (species C), the limiting current obtained due to the oxidation of AH_2 and HX (A and E) will only be affected by k_1 .

2.4. Computation. The simulation procedure utilizes a finite difference method to solve for the steady state solution of each

of the partial differential equations given above. The equations in discretized form are

$$a_{i,j-1}(\lambda_{y1} - \lambda_{y2}) + a_{ij}(-2\lambda_{y1} - \lambda_x - K_1 b_{ij}) + a_{i,j+1}(\lambda_{y1} + \lambda_{y2}) + \lambda_x a_{i-1,j} = 0$$

$$b_{i,j-1} \left(\frac{D_B}{D_A} (\lambda_{y1} - \lambda_{y2}) \right) + b_{ij} \left(-2 \frac{D_B}{D_A} \lambda_{y1} - \lambda_x - K_1 a_{ij} \right) + b_{i,j+1} \left(\frac{D_B}{D_A} (\lambda_{y1} + \lambda_{y2}) \right) + \lambda_x b_{i-1,j} = 0$$

$$c_{i,j-1} \left(\frac{D_C}{D_A} (\lambda_{y1} - \lambda_{y2}) \right) + c_{ij} \left(-2 \frac{D_C}{D_A} \lambda_{y1} - \lambda_x \right) + c_{i,j+1} \left(\frac{D_C}{D_A} (\lambda_{y1} + \lambda_{y2}) \right) + \lambda_x c_{i-1,j} + K_1 a_{ij} b_{ij} - K_2 c_{ij}^2 = 0$$

$$e_{i,j-1} \left(\frac{D_E}{D_A} (\lambda_{y1} - \lambda_{y2}) \right) + e_{ij} \left(-2 \frac{D_E}{D_A} \lambda_{y1} - \lambda_x \right) + e_{i,j+1} \left(\frac{D_E}{D_A} (\lambda_{y1} + \lambda_{y2}) \right) + \lambda_x e_{i-1,j} + K_1 a_{ij} b_{ij} = 0$$

where i and j are the indices in the x and y directions, respectively, and

$$\lambda_{y1} = \frac{1}{(\Delta Y)^2}$$

$$\lambda_{y2} = \frac{1}{2(p-Y)\Delta Y}$$

$$\lambda_x = \frac{PeY(2p-Y)}{2p\Delta X}$$

For the simulation, it is assumed that all electroactive species, AH_2 or HX (A or E), reaching the electrode will be oxidized in a single electron transfer process, giving rise to the boundary condition that at the electrode surface $a = e = 0$. Imposition of the boundary conditions for A, B, C, and E, given in Table 1, allows simultaneous solution of the above set of equations, to give steady state concentration profiles for each species along the whole length of the tube, from which both the theoretical limiting current and ESR signal can be calculated.

The discretized equations given above are nonlinear and therefore must be solved using an iterative method. The method of choice is Newton's method,³⁵ used to solve a system of equations in the form $F(y) = 0$ (see Appendix A). The grid required for solution is only in the spatial dimensions x and y ,

TABLE 1: Boundary Conditions

	species A	species B	species C	species E
electrode surface	$a = 0$	$D_A(\partial a/\partial y) = -D_B(\partial b/\partial y)$	$\partial c/\partial y = 0$	$e = 0$
insulating surface and tube center	$\partial a/\partial y = 0$	$\partial b/\partial y = 0$	$\partial c/\partial y = 0$	$\partial e/\partial y = 0$

and the coarseness of the mesh used affects the accuracy of the result obtained. To ensure that the grid mesh is fine enough that the solution obtained is sufficiently accurate, the limiting current data for the fastest flow rates is compared with the Levich solution. The number of grid points in x and y is increased until the error between the two values is consistently less than 0.1% for each concentration used. The steady state concentration profiles of species A, B, C, and E are evaluated over the cavity length. The profiles of A and E (AH_2 and HX) are used to simulate the limiting current:

$$i_{\text{lim}} = \left(2\pi\rho F n D_A A_{\text{bulk}} \sum_{Nx1}^{Nx2} \frac{a_{i,1} - a_{i,0}}{dy} dx \right) + \left(2\pi\rho F n D_A A_{\text{bulk}} \sum_{Nx1}^{Nx2} \frac{e_{i,1} - e_{i,0}}{dy} dx \right) \quad (9)$$

where $Nx1$ and $Nx2$ correspond to the i values at the upstream and downstream ends of the electrode, respectively. The ESR signal is found using the steady state concentration profile of the ESR-active species C (AHAH_2^{*+}), as described in section 2.2.

To find values for the rate constants k_1 and k_2 , log–log plots of the experimental ESR signal versus flow rate were compared with theoretical curves. The ESR signal data is arbitrary in the sense that the relative, not absolute, number of spins is measured, which means that, in a log–log plot of signal versus flow rate, the data may be shifted by a constant value to allow the theoretical and experimental scales to coincide and to facilitate comparison of the shape of the curves. Once an approximate range of values had been found, the best fit rate constants were converged upon by modeling the ESR signal for the same flow rates as used in the experiments. Then, the differences between experimental and theoretical signal values could be minimized to find the range of rate constant values which gave the best fit for all concentrations used.

3. Experimental Section

3.1. Chemical Reagents. All voltammetric experiments were carried out in acetonitrile (Fisons, dried and distilled) with 0.1 M tetrabutylammonium perchlorate (TBAP, Fluka, puriss. electrochemical grade) as supporting electrolyte. *para*-Chloroaniline, *para*-bromoaniline, *para*-iodoaniline, 2,6-lutidine, and ferrocene were purchased from Aldrich, and *N,N*-dimethyl-*para*-bromoaniline was purchased from Fluka. For the HCl experiments, a 5% mix of HCl in helium was purchased from BOC Gases, Guildford, Surrey, U.K. All reagents used were of the highest commercially available grade and were used without further purification.

3.2. Apparatus. Ex situ voltammetry was carried out on a 0.75 mm diameter gold macrodisk working electrode, with a platinum coil counter and a silver wire pseudoreference electrode (Goodfellow, Cambridge, U.K.). Potential control was achieved using a computer controlled PGSTAT30 potentiostat (Autolab, Eco Chemie, Utrecht, The Netherlands). The gold electrode was polished using 1 and 0.3 μm alumina (Kemet Ltd., U.K.). All solutions were degassed with oxygen-free nitrogen (BOC Gases, Guildford, Surrey, U.K.) for at least 15 min prior to experimentation.

In situ electrochemical ESR experiments were carried out using a gold tube flow cell, the construction and characterization of which has been described previously.²⁶ A platinum gauze counter electrode was positioned downstream of the gold working electrode, and a silver wire reference was placed upstream. As a result of the highly resistive nature of the cell design, it was necessary to attach a 0.1 μF capacitor between the reference and counter electrodes in order to ensure electronic stability under steady state potentiostat control. Fluid motion was maintained using a gravity flow system, employing glass capillaries to achieve slower flow rates. The volume flow rates achieved were in the range 0.1×10^{-3} to $200 \times 10^{-3} \text{ cm}^3 \text{ s}^{-1}$. The gold electrode surface was cleaned between experiments with 3 μm diamond spray (Kemet International Ltd, U.K.), using a tungsten rod to polish it. The electrode length was calibrated at 2.45 mm using a solution of 1 mM ferrocene. The tube diameter (2ρ) was measured at 1.8 mm, using callipers.

ESR spectra were obtained using a JEOL JES-FA100 X-band spectrometer with a cylindrical (TE_{011}) cavity resonator.³⁶ The cell was positioned in this cavity such that x_{gap} , the distance between the upstream edge of the electrode and the end of the sensitive region of the cavity (see Figure 1), measured 2 mm. Cavity tuning was achieved using the JEOL spectrometer software (A-SYSTEM v.1.100, FA-MANAGER v.1.01). To account for variations in cavity Q, signal intensities were measured relative to a standard marker consisting of solid MgO dispersed with Mn^{2+} , inserted into the cavity at the time of measurement. In all of the experiments, a microwave power of 1 mW was used and regular tests were carried out to check that increasing the microwave power increased the ESR signal. Doing so ensured that the system was not power saturated such that the ESR signal intensity gave a direct measure of the number of electrogenerated spins in the cavity.³⁶ All experiments were conducted at $20 \pm 2^\circ\text{C}$.

4. Results and Discussion

4.1. Preliminary Voltammetry. Figure 2 depicts the voltammetric oxidation of 2 mM *para*-chloroaniline dissolved in acetonitrile supported with 0.1 M TBAP, on a 0.75 mm diameter gold disk electrode at a scan rate of 100 mV s^{-1} . The oxidation

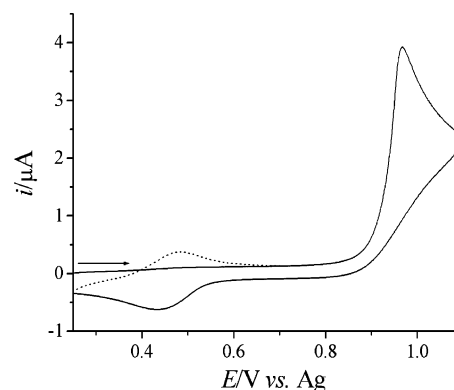


Figure 2. Cyclic voltammetric oxidation of 2 mM *para*-chloroaniline in acetonitrile containing 0.1 M TBAP on a 0.75 mm diameter gold disk electrode. Scan rate, 100 mV s^{-1} . The first scan is represented by the solid line, and part of the second scan is represented by the dotted line.

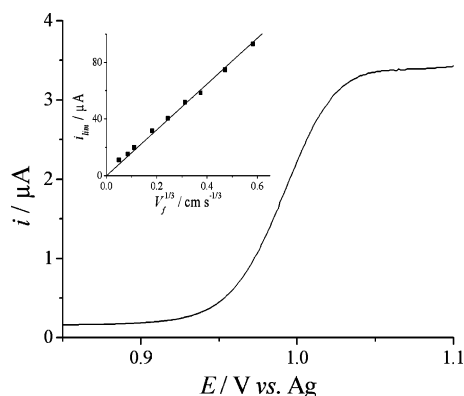


Figure 3. Hydrodynamic voltammogram of 1 mM *para*-chloroaniline in a tubular flow cell at a scan rate of 5 mV s⁻¹ and a flow rate of 10⁻⁴ cm³ s⁻¹. Inset: Levich plot for flow rates in the range 0.1 × 10⁻³ to 200 × 10⁻³ cm³ s⁻¹.

occurs as a single, chemically irreversible wave with a peak potential of 0.95 V versus Ag, with a smaller reductive feature appearing at a potential of 0.45 V versus Ag on the reverse scan. This reduction wave forms part of a quasireversible redox couple which is stable upon subsequent scanning. The voltammetry observed for the corresponding bromo- and iodoaniline derivatives was found to be qualitatively very similar to that of *para*-chloroaniline with peak potentials of 1.03 and 1.02 V, respectively. This behavior is in good agreement with that reported by Farsang and co-workers^{14–18} for the oxidation of *para*-haloanilines in aprotic solvents, where the anodic wave was attributed to the formation of the corresponding radical cation which was shown to be unstable with respect to dimerization on conventional voltammetric time scales. The cathodic feature on the reverse sweep was then ascribed to the two-electron, two-proton reduction of the electrogenerated dimer, the product of which is reoxidized upon subsequent scanning (see Scheme 1).

With the proposed radical mechanism in mind, it was envisaged that an in situ electrochemical ESR study might provide further insight into the follow-up reaction mechanism. ESR has been used previously in the study of the electro-oxidation of substituted anilines, in which the deprotonated radical cations were spin trapped using 2-methyl-2-nitroso propane (MNP), but little mechanistic information was revealed.³⁷

4.2. Electrochemical ESR. The electrochemical ESR was undertaken using a tubular flow cell which has been previously characterized and for which the theory describing the mass transport has been well developed.²⁶ A typical steady state voltammogram depicting the oxidation of 1 mM *para*-chloroaniline, using the tubular flow cell, is shown in Figure 3. Steady state limiting currents were measured at various volume flow rates in the range 0.1 × 10⁻³ to 200 × 10⁻³ cm³ s⁻¹ and were found to scale with $V_f^{1/3}$, as predicted by eq 4 (see Figure 3, inset). Electrolysis of the 1 mM solution at a potential of 1.3 V versus Ag within the ESR cavity yielded only a very weak spectrum, even at high modulation widths, which diminished upon an increase in the flow rate. The low signal intensity would suggest that the paramagnetic species being detected was unstable on the experimental time scale (or was not being generated in very appreciable quantities), but upon increasing the aniline concentration, stronger ESR signals were observed and more conclusive hyperfine spectra could be obtained. Figure 4a shows the ESR spectrum observed upon electrolysis of a 20 mM solution of *para*-chloroaniline, at a magnetic field modulation width of 0.4 mT, which displays a coarse structure

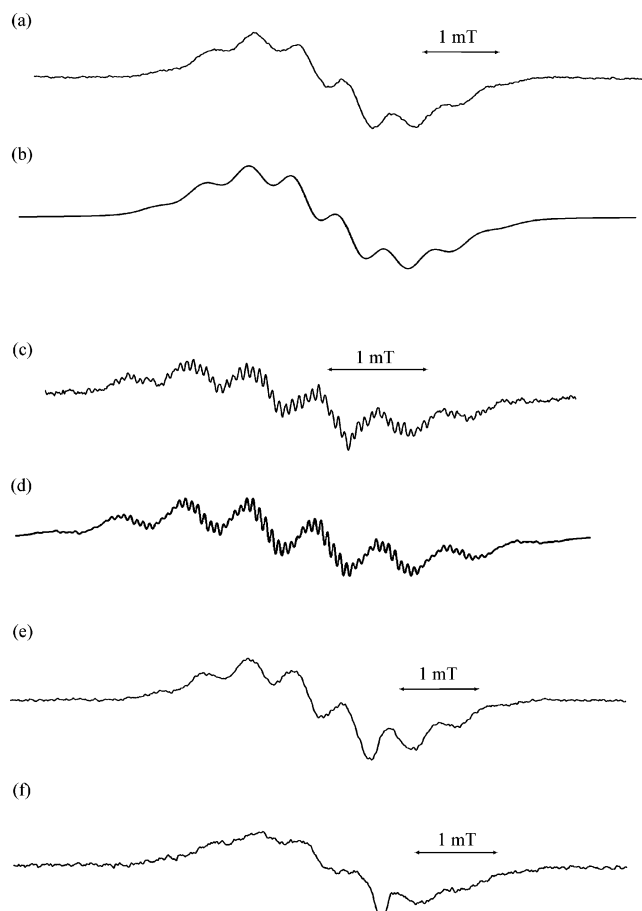


Figure 4. (a) Experimental ESR spectrum obtained from a 20 mM solution of *para*-chloroaniline, flowing at 6 × 10⁻³ cm³ s⁻¹ and potentiostated at 1.3 V vs Ag using a modulation width of 0.4 mT (5 × 4 min acquisitions). (b) Simulated spectrum obtained using hyperfine coupling constants for the ADPA^{•+} radical cation⁴⁰ and a line width of 0.20 mT. (c) Experimental spectrum as in part a at a modulation width of 0.1 mT (5 × 4 min acquisitions). (d) Simulated spectrum as in part b using a line width of 0.07 mT. (e) Experimental ESR spectrum obtained from a 10 mM solution of *para*-bromoaniline, flowing at 6 × 10⁻³ cm³ s⁻¹ and potentiostated at 1.3 V vs Ag using a modulation width of 0.2 mT (5 × 4 min acquisitions). (f) Experimental spectrum as above for 5 mM *para*-iodoaniline.

consisting of eight lines, broadened by overmodulation. Upon reducing the modulation width to 0.1 mT, the spectrum retains its overall structure, but each of the broad lines demonstrates a further level of hyperfine splitting due to the higher resolution (Figure 4c). The relatively poor signal-to-noise ratio of the spectra shown, in comparison to that demonstrated for the stable paramagnetic species described in section 4.5 (vide infra), suggests that the observed radical species have a relatively short lifetime, but there is also evidence of spin–lattice broadening as a consequence of the high substrate concentrations being used. ESR spectra obtained upon the oxidation of *para*-bromoaniline and *para*-iodoaniline were similarly fairly weak but qualitatively very similar to those described above (Figure 4e and f).

To elucidate the identity of the electrogenerated radical species from the observed ESR spectra, a series of spectral simulations were carried out based on known hyperfine coupling constants for stable paramagnetic aniline derivatives.^{37–40} Initially, attempts were made to simulate the spectrum of the primary radical cation of the *para*-haloanilines; analysis of the molecular structure of the radical cation would suggest a 1:1:1 line splitting due to the ¹⁴N atom ($I = 1$), a 1:2:1 splitting due to the two equivalent amine protons, and two further 1:2:1

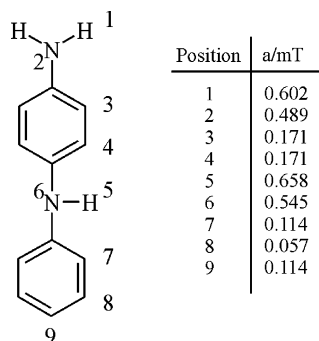


Figure 5. Structure of *para*-aminodiphenylamine, with documented hyperfine coupling constants for its radical cation, ADPA^{•+}.⁴⁰

splittings due to the two sets of two equivalent ring protons ($I = 1/2$), but none of the halogen atoms are likely to contribute to the hyperfine structure of the ESR spectra due to spin relaxation arising from their significant electric quadrupole moments.³⁶ However, attempts to simulate the spectra on this basis, using a range of line widths, were unsuccessful, suggesting that the paramagnetic species being detected was not the primary radical cation. This was also found when attempting to simulate the spectrum for a deprotonated radical cation. Upon reviewing the literature, it was noted that Petr and Dunsch^{20,41} had observed a similar spectrum to that in Figure 4a for the radical cation of *para*-aminodiphenylamine (ADPA^{•+}, see Figure 5), a known intermediate in the anodic oxidation of aniline, implying that the ESR spectrum of an electrogenerated paramagnetic dimer product should be considered. Using the hyperfine coupling constants reported by Male and Allendoerfer⁴⁰ for ADPA^{•+} in aqueous solution, shown in Figure 5, spectra were simulated which very closely resemble the experimental spectra in Figure 4a and c, and are depicted in Figure 4b and d at two different line widths. It should be noted that the para ring proton coupling constant was omitted from the simulation, since a halogen atom likely occupies this position, as will become apparent when considering the mechanism of dimer formation (vide infra). Inspection of the hyperfine coupling constants used reveals that the two ¹⁴N atoms and the three amino protons are responsible for the broad eight-line structure of the spectra shown in Figure 4a and b, whereas the ring protons cause a much smaller splitting which is visible on the higher resolution spectra (Figure 4c and d) and, as such, the presence of a para ring proton splitting does not alter the simulated spectrum significantly.

Scheme 2 depicts a possible mechanism, which could rationalize the ESR observations discussed above. The electrogenerated radical cation is thought to undergo a deprotonation step, yielding the neutral radical, as was suggested by Farsang et. al.,^{14–18} and this reacts with a parent haloaniline molecule, present in a large excess under our experimental conditions, in a “head-to-tail” sense. The adduct formed can then collapse with the loss of a halide anion to yield the para halogenated *para*-aminodiphenylamine radical cation, whose structure is not inconsistent with the ESR spectra observed. As mentioned above, the observed radical species shows signs of instability, as suggested by the weak signal intensity, and although the exact fate of the suggested dimer radical cation is unknown, based on the chemistry of aqueous ADPA^{•+},^{20,41} it is possible that it combines with another radical cation on the experimental time scale to give a non-paramagnetic product, which could rationalize the low intensity ESR signals observed. The mechanism proposed differs from that postulated by Farsang et. al.,^{14–18} in which the electrogenerated radical cation reacts with a neutral

radical, formed via deprotonation of the radical cation, to yield the dimer in a higher, non-paramagnetic oxidation state.

To further verify the role of the observed radical in the overall reaction pathway and to probe the kinetics of the proposed mechanism, the ESR signal intensity was measured as a function of flow rate, steady state limiting current, and *para*-haloaniline concentration. The ESR signal intensity was measured relative to that of a standard Mn²⁺ marker and recorded as the peak-to-peak height of the overmodulated signal, taken at a modulation width of 2 mT. It has been well established that, within a tubular electrode cell of the design employed in this work, for a stable radical species, the ESR signal intensity, S , the limiting current, i_{lim} , and the volume flow rate, V_f , behave according to the following relationship:^{25,26}

$$\frac{S}{i_{\text{lim}}} \propto \frac{1}{V_f^{2/3}} \quad (10)$$

It is therefore informative to plot the log of the current normalized signal intensity, S/i_{lim} , against the log of V_f , since deviation from this $-2/3$ power law is indicative of radical instability. For example, in the simple case where a radical species is generated at the electrode surface and undergoes radical–radical dimerization (i.e., an EC_{dim} reaction), such a log–log plot may show linearity at fast flow rates with a gradient tending to $-2/3$ but curving below this slope as the flow rate is decreased. This general behavior can be rationalized by considering a tradeoff between radical lifetime and residence time in the ESR cavity; at fast flow rates, electrogenerated radicals appear stable on the experimental time scale, but as the flow rate is reduced, the radicals are able to react before they have left the ESR cavity, leading to a reduced signal intensity.

Experimental measurements were carried out by electrolyzing solutions of *para*-chloro- and *para*-bromoaniline, at concentrations in the range 5 to 30 mM, at 1.3 V versus Ag, and measuring both S and i_{lim} at flow rates ranging from 0.1×10^{-3} to $30 \times 10^{-3} \text{ cm}^3 \text{ s}^{-1}$. The experimental data recorded are depicted in Figure 6. In each case, $\log(S/i_{\text{lim}})$ appears to vary approximately linearly with $\log(V_f)$ at high flow rates for each concentration, the slopes of which are reported in Table 2, but as the flow rate decreases, $\log(S/i_{\text{lim}})$ tails off, with the deviation becoming more evident with increasing concentration. The more pronounced signal reduction observed at higher haloaniline concentration is expected if the paramagnetic species decays with second-order kinetics; that is, increasing the concentration of the radical dimer increases the rate of its bimolecular consumption. Although *para*-iodoaniline behaved similarly in its ESR signal to the chloro and bromo derivatives, it was difficult to obtain reproducible signal intensity data, probably as a result of some electrode fouling and precipitation effects which were observed during electrolysis.

Qualitatively, the curved nature of the log–log plots in Figure 6 can be rationalized by the arguments above for a simple EC_{dim} process. However, inspection of the gradients in Table 2, which were recorded in the “fast” flow rate limit ($V_f > 6 \times 10^{-3} \text{ cm}^3 \text{ s}^{-1}$), reveals a significant deviation from the expected slope of $-2/3$ for such a mechanism. This rather unexpected behavior would suggest a mechanism more complex than this EC_{dim} reaction and might therefore support a reaction scheme such as that depicted in Scheme 2. To investigate this possibility more rigorously, it was necessary to attempt to model the signal intensity data using simulations based on the theory developed in section 2, but before any modeling could be carried out, a number of mechanistic considerations needed to be addressed.

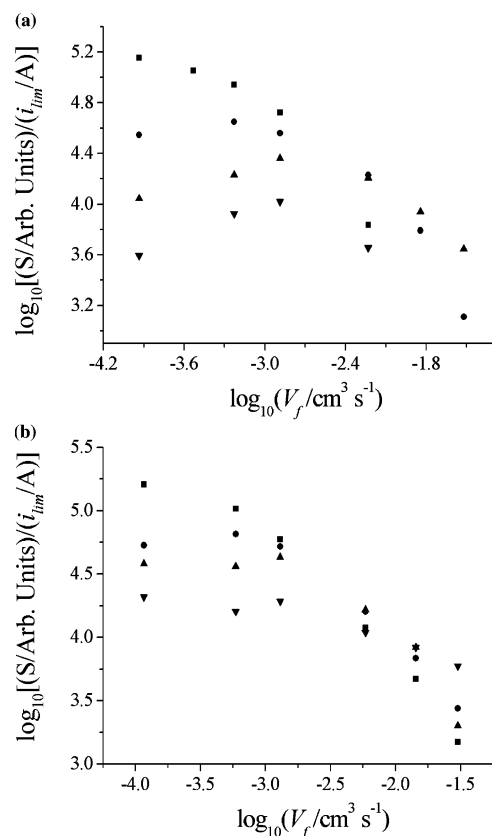


Figure 6. Current normalized ESR signal intensity, S/i_{lim} , as a function of volume flow rate, V_f , for (a) *para*-chloroaniline (■, 5 mM; ●, 10 mM; ▲, 20 mM; ▼, 30 mM) and (b) *para*-bromoaniline (■, 5 mM; ●, 10 mM; ▲, 15 mM; ▼, 20 mM).

TABLE 2: Slopes Measured from Plots in Figure 6 ($V_f > 6 \times 10^{-3} \text{ cm}^3 \text{ s}^{-1}$)

	5 mM	10 mM	15 mM	20 mM	30 mM
<i>para</i> -chloroaniline	-1.12	-1.13		-0.76	-0.43
<i>para</i> -bromoaniline	-1.15	-0.92	-0.92	-0.37	

4.3. Mechanistic Aspects. There are two important features of the mechanism depicted in Scheme 2 which have not yet been considered, namely, the details of the initial deprotonation step and the fate of the halide anion ejected in the latter stages of the dimerization. These features, which are also aspects of the mechanism proposed by Farsang et al.,¹⁴ are important when considering the contributions to the anodic current. Each of these will now be discussed in turn.

4.3.1. Voltammetry in the Presence of a Base. A number of species are present in the solution that are capable of carrying out the deprotonation step, such as the parent aniline, the acetonitrile solvent, or any of the basic products formed as a result of the electrodimmerization reaction, such as the halide anions present in low concentration in the reaction layer. There is documented evidence to suggest that acetonitrile can act as a base to yield CH_3CNH^+ ,^{42,43} although it is probably more convenient here to consider this acid–base reaction as being proton solvation, since the acetonitrile is present in such an excess. However, amines and halide anions (chloride and bromide in particular, vide infra) are considered to be relatively strong bases in aprotic solvents,^{42–45} so neither can be ignored as participants in this step. It has been postulated that anilines in a protonated state cannot be oxidized electrochemically,^{3,4,16} and thus, it is important to know whether the parent molecule acts as a base, since this process would diminish the concentration of electroactive *para*-haloaniline at the electrode surface.

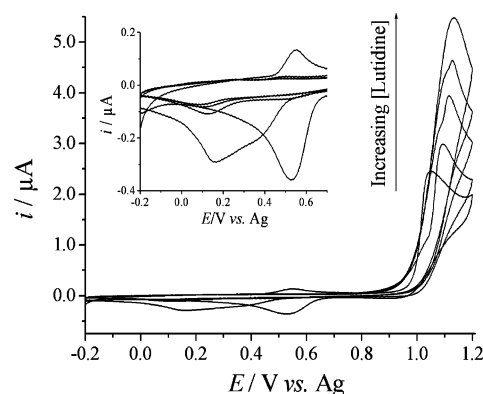


Figure 7. Cyclic voltammetric oxidation of 2 mM *para*-chloroaniline (50 mV s^{-1}) with additions of 2,6-lutidine (0, 0.5, 1.5, 2.0, and 3.0 mM).

To interrogate the mechanism of radical cation deprotonation, the voltammetry of *para*-chloroaniline and *para*-bromoaniline was examined in the presence of the non-nucleophilic base 2,6-lutidine, as was previously investigated for these compounds in DMF by Farsang et al.¹⁴ The $\text{p}K_a$ of protonated lutidine in water has been measured at 6.7,⁴⁶ whereas those for protonated *para*-chloro- and *para*-bromoaniline have been reported as 4.0 and 3.9, respectively,⁴⁷ which would suggest that, in acetonitrile, lutidine is a stronger base than either parent aniline.

Figure 7 depicts the voltammetric oxidation of 2 mM *para*-chloroaniline at 50 mV s^{-1} with various additions of lutidine, where it can be seen that the peak current of the anodic wave increases with lutidine concentration and the wave shifts to more positive potentials, with the formation of a preoxidative shoulder. At higher lutidine concentrations, the oxidative shoulder coalesces with the primary peak to form a slightly broadened anodic wave which continues to increase in magnitude up until the addition of approximately 5 mM lutidine (2.5 equiv), after which the addition of further base has little effect. This is in quite significant contrast to the behavior reported by Farsang et al., who observed no change in peak currents and a shift to more negative potentials upon the addition of lutidine to *para*-chloroaniline in DMF,¹⁴ suggesting that the influence of the solvent is a crucial consideration. The observed increase in peak current upon the addition of base can be rationalized if, in the mechanism postulated in Scheme 2, the parent aniline molecules carry out the initial deprotonation step; the addition of base essentially prevents parent molecules from being “deactivated” with respect to oxidation by protonation, increasing the effective concentration and therefore maximizing the peak current. The shift of the anodic peak to more positive potentials on lutidine is also typical of such an $E_{\text{rev}}C$ process, such that, upon the addition of lutidine, the deprotonation step is no longer facilitated by the presence of basic *para*-chloroaniline. The presence of a shoulder on the voltammetric wave in the presence of lutidine is likely the result of a depletion effect, in which the added lutidine is initially “titrated” against the electrogenerated *para*-chloroaniline radical cations (i.e., one wave corresponds to the lutidine catalyzed process, and the other, to the *para*-chloroaniline facilitated process). Once the lutidine is in sufficient excess (5 mM in this case), the deprotonation is purely due to lutidine such that all of the *para*-chloroaniline is free to be oxidized. Qualitatively very similar behavior is observed for *para*-bromoaniline, but much more lutidine is required (up to 30 mM, 15 equiv) before the peak current approaches its maximum, suggesting that the bromo derivative competes more significantly with lutidine in the deprotonation stage than *para*-chloroaniline. This implies that lutidine is a stronger base than

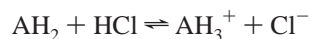
para-chloroaniline but comparable in basicity to *para*-bromoaniline in acetonitrile.

Upon close inspection of the reverse waves (Figure 7, inset), it appears that the addition of base imposes chemical irreversibility onto the dimer redox couple, with the reduction wave shifting to more negative potentials and decreasing in magnitude. Moreover, ESR experiments in the presence of lutidine yielded no appreciable signals, which is understandable, since deprotonation of the dimer radical cation likely results in its destabilization with respect to dimerization (the kinetics of radical–radical coupling are probably faster than the kinetics of radical cation–radical cation coupling, and thus, in the presence of base, this chemical step may be visible on the ESR experimental time scale). The underlying conclusion to be drawn from the above observations, however, remains that, in the absence of a base, the primary radical cation deprotonation step must be carried out by the parent *para*-haloaniline substrate.

4.3.2. Fate of the Halide Anion. In the mechanism proposed by Bacon and Adams¹³ for the anodic oxidation of *para*-chloroaniline in aqueous solution, a Cl[−] ion is ejected during the dimerization process. If we consider this mechanism taking place in aprotic solvents, where the electrochemical oxidation of chloride is possible at potentials less positive than the oxidation potential of *para*-chloroaniline, then this additional process may contribute to some extent to the anodic current, as was discussed by Farsang et al.^{14–19} However, it has been shown that, in acetonitrile, the equilibrium constant for the following reaction:



is close to 10^{−9} mol dm^{−3} (and 10^{−6} mol dm^{−3} for HBr),⁴⁵ and thus, under the experimental conditions employed in this work, the ejected chloride anion is a very strong base and is likely to leave in a protonated form. On the other hand, one cannot rule out the deprotonation of HCl as a result of the basic aniline environment, so a series of experiments was carried out to probe the following equilibrium:



where AH₂ and AH₃⁺ are the neutral and protonated *para*-chloroaniline molecules, respectively.

This equilibrium was investigated by way of UV–visible spectroscopy, in which HCl was introduced to a solution of *para*-chloroaniline in acetonitrile. It was envisaged that, since the spectra of the neutral and protonated *para*-chloroaniline species differ,⁴⁸ this would give a measure of their relative concentration in solution and allow the approximation of the equilibrium constant. The details of these experiments and the subsequent calculations are outlined in Appendix B, where the equilibrium constant, *K*_{eq}, is defined as

$$K_{\text{eq}} = \frac{[\text{AH}_3^+][\text{Cl}^-]}{[\text{AH}_2][\text{HCl}]}$$

From the UV–vis spectroscopic data, under equimolar concentrations of AH₂ and HCl, *K*_{eq} was estimated as 0.01, suggesting that the above equilibrium lies to the left-hand side, consistent with the chloride anion being a significantly stronger base than *para*-chloroaniline. Although we cannot be certain as to the exact proton motion during the course of the reaction mechanism, we can conclude from the above observation that

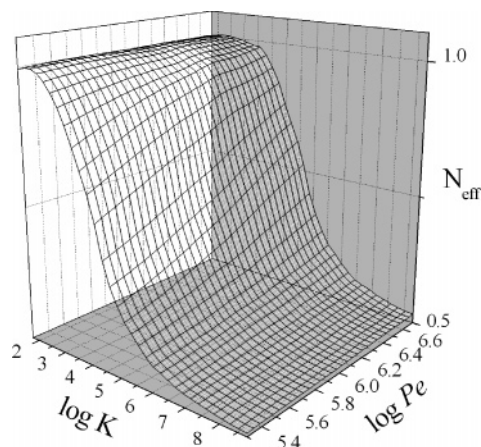


Figure 8. Working surface showing the value of *N*_{eff} as a function of *Pe* and *K*₁.

the thermodynamics of the system dictate that the expelled chloride must ultimately be protonated in the overall scheme. It is possible that the oxidation of the expelled HCl, rather than that of Cl[−], contributes to the anodic current, and thus, this needs to be considered when modeling the ESR and voltammetric data. Attempts were made to investigate the voltammetric behavior of HCl dissolved in acetonitrile, but such experiments proved unfruitful due to poor reproducibility as a result of electrode passivation; thus, the mechanism of HCl oxidation remains speculative. The suggestion that the dimerization reaction occurs with the loss of HCl at first appears inconsistent with Scheme 2; it was concluded from the ESR spectral simulations that three amino protons were present in the dimeric species being detected, but the above observations suggest that one of these protons must leave with the ejected chloride ion to yield a neutral radical dimer. However, if the electrogenerated haloaniline radical cation is deprotonated by the parent haloaniline and then, rather than reacting with the neutral parent, reacts with the now protonated parent, possibly within the same solvent cage, the dimer generated after the loss of HCl has the three amino protons, as suggested by the ESR spectral simulations. Alternatively, the protonated parent could donate a proton at a later stage in the reaction, but in any case, the formation of the proposed dimer is not inconsistent with the loss of HCl in the overall reaction scheme.

With the above mechanistic considerations in mind, the ESR and voltammetric data were modeled in order to probe the kinetics of the follow-up chemistry of the electrogenerated haloaniline radical cations.

4.4. Simulation of ESR Data. **4.4.1. Limiting Current Data and *N*_{eff}.** Due to the nature of the mechanism, where the species produced at the electrode, AH₂^{•+}, reacts with the parent, AH₂, the current passed at the electrode due to the oxidation of AH₂ is dependent upon the rate of this step in the process. Thus, the effective number of electrons transferred, *N*_{eff}, is equal to 1 if there is no homogeneous reaction taking place and will have its limiting value at 0.5 for a very fast reaction. The current is also higher if a faster flow rate is used, due to the increased convective mass transport to the electrode. Figure 8 shows the working surface for the value of *N*_{eff} with changing normalized rate constant, *K*₁, and changing flow rate or Peclet number, *Pe*.

4.4.2. Fitting of ESR Signal Data. For the simple case where a stable ESR-active species is produced at the electrode under conditions where the Lévêque approximation is valid,²⁵ the ESR signal has been shown to be proportional to *V*_f^{−1/3} (this follows from substitution of the Levich relation into eq 10). If our system

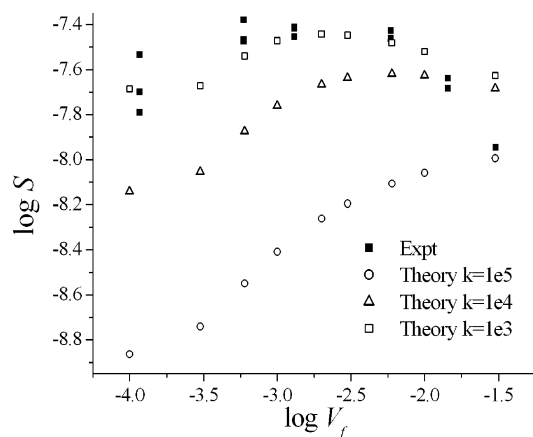
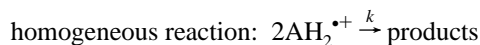


Figure 9. Theoretical ESR signal vs flow rate data compared with experiment using 10 mM chloroaniline, for the simple dimerization scheme (section 4.3.2).

TABLE 3: Simulation Parameters

x_e	0.245 cm
x_{gap}	0.2 cm
ρ	0.09 cm
D_A, D_B, D_C	$2.1 \times 10^{-5} \text{ cm}^2 \text{ s}^{-1}$
D_E	$5 \times 10^{-5} \text{ cm}^2 \text{ s}^{-1}$

is modeled as the production of a radical cation, $AH_2^{\bullet+}$, followed by a dimerization process,



then the $V_f^{-1/3}$ dependence is still observed for the fastest flow rates. Some sample theoretical results for this simple dimerization scheme are shown in Figure 9 compared with the experimental data for 10 mM chloroaniline. It can be seen that the gradient at high flow rates approaches $-1/3$ for the lower values of the rate constant, k , for the dimerization but does not reach the much steeper gradient observed experimentally. Therefore, the system cannot be simplified to such an extent.

As established above in sections 4.2 and 4.3, a more suitable model to describe the haloaniline system is that in which the original electrogenerated radical cation, $AH_2^{\bullet+}$, reacts with the starting material, AH_2 , to ultimately form $AHAH_2^{\bullet+}$ and HX, with $AHAH_2^{\bullet+}$ subsequently lost through a second-order dimerization process (see Scheme 3). If the ESR signal registered experimentally is that due to the paramagnetic $AHAH_2^{\bullet+}$, it will not exhibit the $V_f^{-1/3}$ dependence expected if the species $AH_2^{\bullet+}$ were responsible for the measured spectrum, such that the gradient observed in the log–log plot of ESR signal against flow rate is steeper than the value of $-1/3$ predicted by the simplified model.

The program modeling Scheme 3, applied to the ESR data, was used to find the range of values for the rate constants k_1 and k_2 which gave the best fit to the experimental data (section

2.4) using bromo- and chloroaniline as the starting material, AH_2 (species A), at various concentrations. The parameters used are listed in Table 3; lengths and other parameters quoted are defined in Figure 1. The fitting process was repeated for each species and for each concentration of starting material used, and the values of k_1 and k_2 obtained were in good agreement, as shown in Table 4. A sample of the data fitting for the chloroaniline species is given in Figure 10, and it can be seen that the model used for simulation of the experimental data both fits with the steep gradient at high flow rates and follows the curve shape as lower flow rates are used.

Values for k_1 can also be estimated by analyzing just the limiting current versus flow rate data. From these results, shown in Figure 11 and Table 4, the value for k_1 appears to be much higher than that found from analysis of the ESR signal data. This can be explained by comparison of the simplified theoretical reaction scheme (Scheme 3) with the chemical mechanism (Scheme 2), bearing in mind the observations made in section 4.3.. The homogeneous step for the formation of $AHAH_2^{\bullet+}$ actually occurs in multiple stages, beginning with a proton exchange:



where AH^{\bullet} is the neutral deprotonated radical. The first step in this mechanism affects the limiting current response, as it involves the electroactive species, AH_2 , and it would be expected that this deprotonation stage occurs faster than the proceeding steps. The later stages, such as the coupling of the neutral radical, AH^{\bullet} , with the parent, AH_2 (or alternatively the protonated parent, AH_3^+ , as discussed in section 4.3.2), occur at a slower rate, and it is these processes which control the formation of the radical species, $AHAH_2^{\bullet+}$, downstream of the electrode surface and hence the ESR response. We therefore have conflicting kinetic parameters, since the limiting current response describes the loss of AH_2 at the electrode but the ESR response describes the formation and loss of $AHAH_2^{\bullet+}$ downstream (since the electrode is positioned close to the upstream edge of the ESR cavity), which take place at measurably different rates.

Since Scheme 3 alone cannot rationalize these observations, it was necessary to analyze the voltammetric behavior more rigorously in order to reconcile the above conflict. An important feature of the above rationalization is that the expelled HCl can only be present downstream of the electrode, and thus, there should be no contribution to the anodic limiting currents due to its electro-oxidation. In an attempt to verify this, and the kinetic parameters obtained using the tubular flow cell, the quiescent gold macrodisk voltammetry was modeled using Digisim.

4.5. Digisim Modeling. The preliminary voltammetry obtained for the oxidation of *para*-chloroaniline was first modeled using Digisim according to the mechanism described in Scheme 3, with and without anodic current contributions from the HCl oxidation step. From this, it was found that significant additional

TABLE 4: Rate Constants from Fitting of I_{lim} and ESR Signal Data

species and concentration	k_1 from i_{lim} data ($\text{cm}^3 \text{ mol}^{-1} \text{ s}^{-1}$)	k_1 from ESR signal data ($\text{cm}^3 \text{ mol}^{-1} \text{ s}^{-1}$)	k_2 from ESR signal data ($\text{cm}^3 \text{ mol}^{-1} \text{ s}^{-1}$)
10 mM chloroaniline	5×10^6 to 5×10^7	5×10^3 to 1×10^4	1×10^3 to 1×10^4
20 mM chloroaniline	1×10^7 to 1×10^8	8×10^3 to 2×10^4	5×10^3 to 1×10^4
30 mM chloroaniline	1×10^7 to 1×10^8	5×10^3 to 1×10^4	5×10^3 to 1×10^4
10 mM bromoaniline	5×10^6 to 5×10^7	5×10^3 to 1×10^4	5×10^3 to 1×10^4
15 mM bromoaniline	1×10^7 to 1×10^8	5×10^3 to 1×10^4	5×10^3 to 1×10^4
20 mM bromoaniline	1×10^7 to 5×10^7	8×10^3 to 2×10^4	5×10^3 to 2×10^4

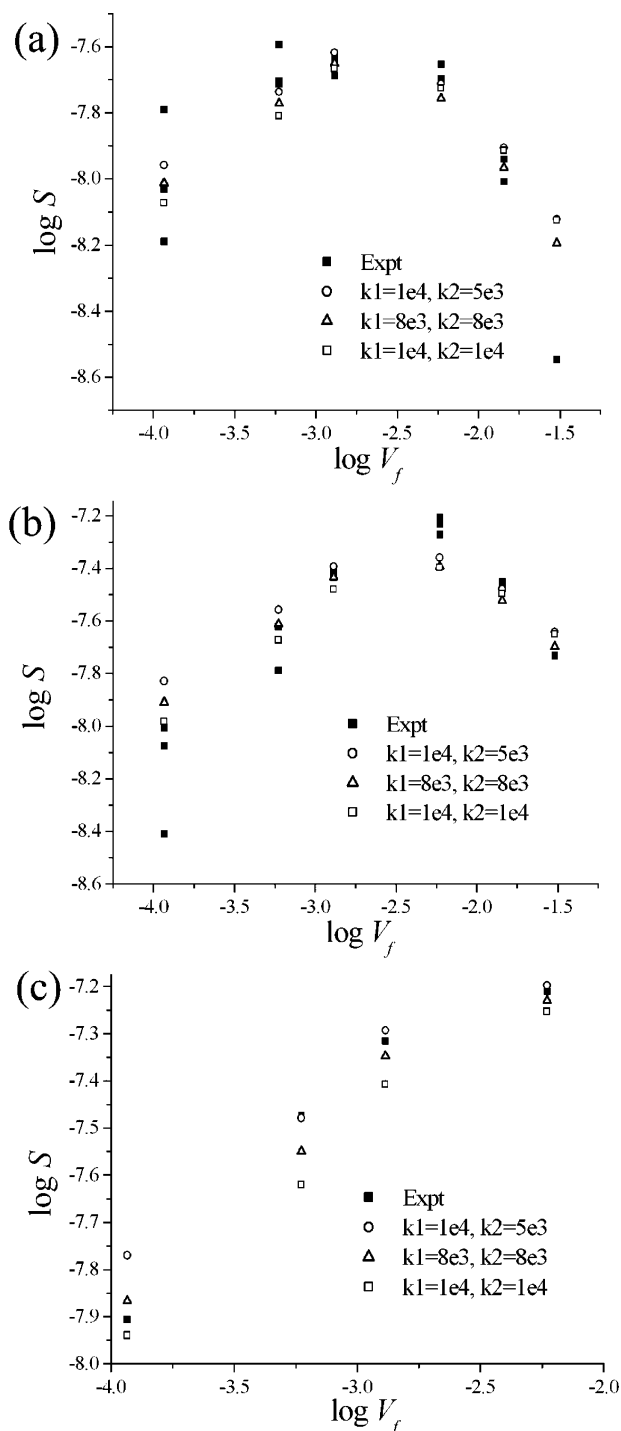


Figure 10. Theoretical \log signal vs $\log V_f$ plots (V_f in units of $\text{cm}^3 \text{s}^{-1}$) for various k_1 and k_2 values compared with experimental data for (a) 10 mM, (b) 20 mM, and (c) 30 mM chloroaniline.

anodic contributions were necessary in order to simulate the peak currents using reasonable values for the substrate diffusion coefficient (using the Wilke–Chang approximation,⁴⁹ the diffusion coefficient of *para*-chloroaniline in acetonitrile is estimated at $2.1 \times 10^{-5} \text{ cm}^2 \text{s}^{-1}$). This is consistent with the observations made in previous investigations, where larger measured values of n were attributed to the oxidation of ejected halide anions,^{14–19} but is inconsistent with the rationalization given above for the discrepancies in the deduced kinetic parameters. This led to the suggestion that the modeled mechanism was not the dominant pathway, as suggested by the low signal intensities measured, but ran parallel with an

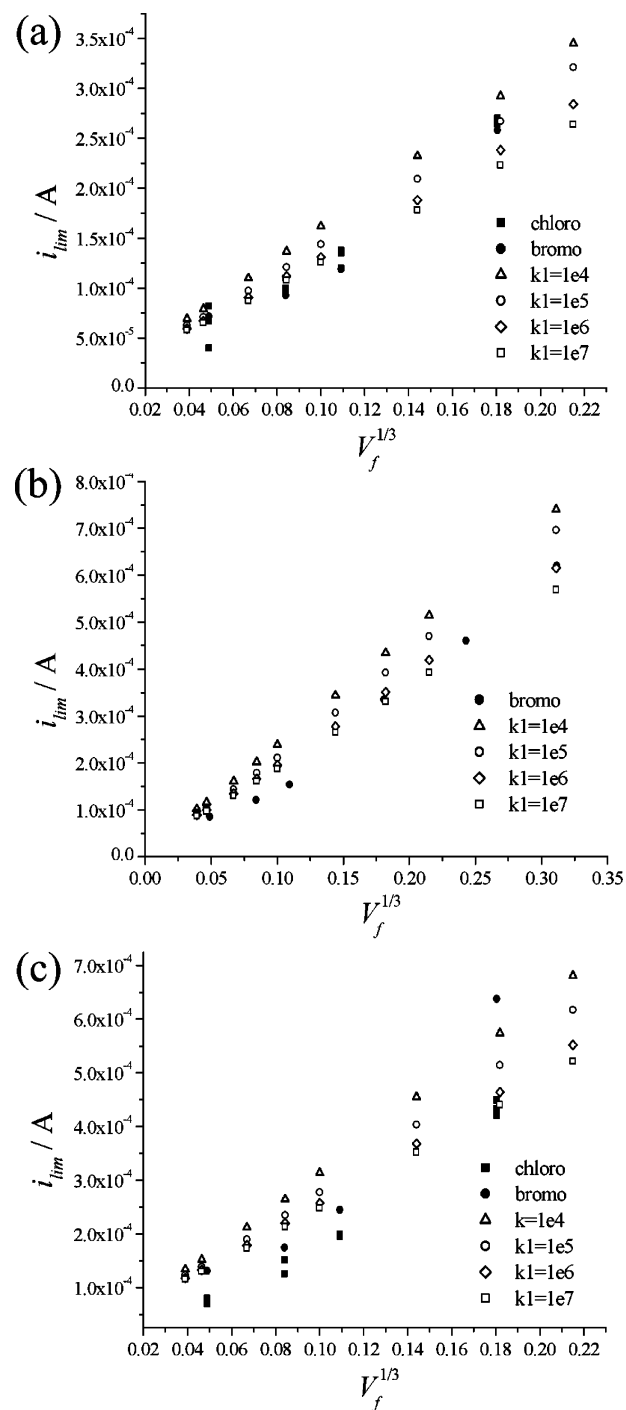


Figure 11. Theoretical limiting current data for various values of k_1 compared to experimental bromoaniline and chloroaniline data: (a) 10 mM; (b) 15 mM; (c) 20 mM (V_f in units of $\text{cm}^3 \text{s}^{-1}$).

alternative reaction scheme in which HCl is generated quickly and oxidized at the electrode surface, thus contributing to the anodic current. Such a suggestion is conceivable if one considers the multiple fates of the neutral haloaniline radical formed via deprotonation of the radical cation; the haloaniline radical could react with a parent aniline molecule (protonated or not), as in Scheme 2, or could couple with another electrogenerated radical cation, as in Scheme 1. We know from the ESR signal data that the former process is slow and so any HCl generated by this cannot affect the voltammetric signal, but if the latter process occurs very quickly and dominates over the former, then HCl may be produced in significant quantities at the electrode surface and can therefore contribute to the anodic current. With

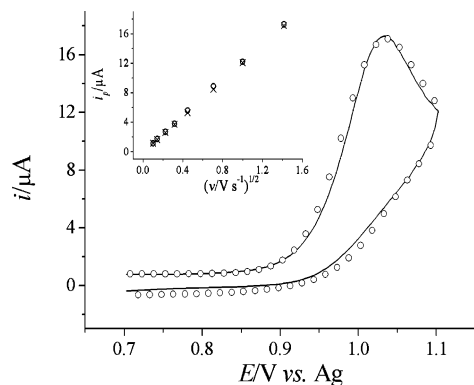
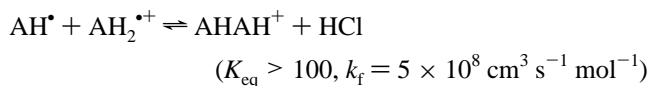
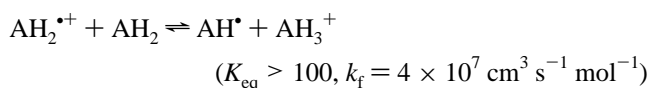
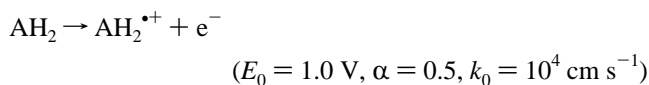


Figure 12. Experimental (—) and simulated (○) voltammograms for the voltammetric oxidation of 2 mM *para*-chloroaniline at 2000 mV s⁻¹. Inset: experimental (○) and simulated (×) peak currents as a function of scan rate, v . See text for Digisim parameters (the additional parameters used were a 0.4 μ F capacitance and a 1 k Ω uncompensated resistance).

this in mind, the voltammetric signals were modeled under the following scheme, using the parameters shown below:



It is also possible that the transient neutral radical, AH^\bullet , can be further oxidized at the electrode surface, but we found no evidence to suggest this, and since no such process been reported in the literature, this notion was not considered further. A diffusion coefficient of $2.3 \times 10^{-5} \text{ cm}^2 \text{ s}^{-1}$, was used for the monomer aniline species (AH_2 , $\text{AH}_2^{\bullet+}$, AH^\bullet , and AH_3^+) in good agreement with the Wilke–Chang approximation,⁴⁹ and $1.8 \times 10^{-5} \text{ cm}^2 \text{ s}^{-1}$ was used for that of the dimer species, AHAH_2^+ , as reported by Timofeeva et. al. for *para*-aminodiphenylamine in acetonitrile.⁵⁰ The HCl oxidation was modeled as a simple single electron transfer with a sufficiently negative E_0 , chosen such that the process was diffusion controlled under all conditions, and a value of $5 \times 10^{-5} \text{ cm}^2 \text{ s}^{-1}$ was used for the diffusion coefficient for HCl and its oxidation product (this relatively high value is not unreasonable for a diatomic molecule such as HCl in acetonitrile). Although the details of this process are uncertain, it is possible that it involves dissociation of the “HCl”⁺ product into a proton and a chlorine atom which adsorbs on the electrode surface. A typical fit is shown in Figure 12 for the 2000 mV s⁻¹ oxidation of 2 mM *para*-chloroaniline, where good agreement between experiment and simulation is observed for the forward wave. A good correlation was observed between experimental and simulated oxidative peak currents, over a range of scan rates (see Figure 12, inset).

The value $4 \times 10^7 \text{ cm}^3 \text{ s}^{-1} \text{ mol}^{-1}$ for the forward rate constant of the initial homogeneous step is in relatively good agreement with that obtained from simulation of the flow cell limiting current data, suggesting that both sets of voltammetry are consistent with the mechanism outlined above, whereas the ESR data supports the mechanism depicted in Scheme 2. This

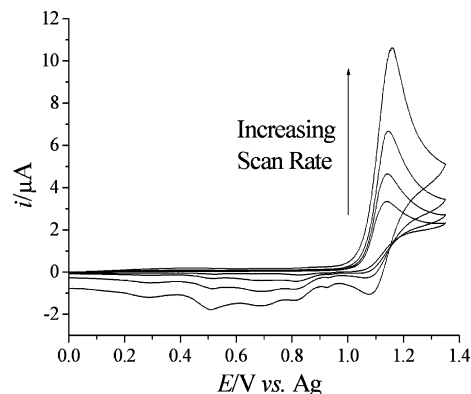


Figure 13. Cyclic voltammetric oxidation of 2 mM *N,N*-dimethyl-*para*-bromoaniline in acetonitrile containing 0.1 M TBAP on a 0.75 mm diameter gold disk electrode at scan rates of 50, 100, 200, and 500 mV s⁻¹.

suggests, therefore, that there are in fact two mechanistic pathways following the initial proton transfer, one which occurs quickly and the effects of which are visible on the voltammetric time scale and another which occurs slowly to yield the paramagnetic dimer downstream of the hydrodynamic electrode.

Modeling of the experimental disk voltammetry for *para*-bromoaniline was successfully achieved also using the same set of parameters except $E_0 = 1.1 \text{ V}$ for the first electrode process, $k_f = 1.25 \times 10^8 \text{ cm}^3 \text{ s}^{-1} \text{ mol}^{-1}$ for the second of the two homogeneous steps, and $D = 2.1 \times 10^{-5} \text{ cm}^2 \text{ s}^{-1}$ for the monomeric aniline species.

4.6. *N,N*-Dimethyl-*para*-bromoaniline. It is evident from the observations discussed above, and those reported previously,^{14–19} that N-deprotonation of the *para*-haloaniline radical cations plays a crucial role in the follow-up chemistry, suggesting that a different behavior might be observed for an N-methylated aniline derivative, and thus, this was investigated as an interesting aside. Figure 13 depicts typical cyclic voltammograms for 2 mM *N,N*-dimethyl-*para*-bromoaniline on a gold macrodisk at a range of scan rates. At scan rates below 200 mV s⁻¹, the oxidation at 1.15 V versus Ag is chemically irreversible, with a number of cathodic waves on the reverse sweep, but at faster scan rates, a back peak emerges which is associated with the anodic wave, consistent with an EC mechanism in which the homogeneous reaction kinetics can be out-run at conventional scan rates. The system approaches full reversibility at scan rates in the order of 50 V s⁻¹ at which the ratio of cathodic to anodic peak current is close to unity. Since, in the work by Amatore,¹⁴ scan rates in excess of 10^4 V s^{-1} were required before the oxidation of *para*-bromoaniline became chemically reversible, it would appear that the N-methylation of this compound brings a significant degree of stability to the electrogenerated radical cations, increasing their lifetime by orders of magnitude. The voltammetry observed here is consistent with that reported by Hand and co-workers⁵¹ for the anodic oxidation of *N,N*-dimethyl-*para*-bromoaniline at platinum, where the multiple cathodic waves were attributed to the reduction of the *N,N,N',N'*-tetramethylbenzidine dication (a product of “tail-to-tail” coupling of electrogenerated radical cations) in addition to molecular bromine, generated during the course of electrolysis (vide infra). The longer lifetime of the *N,N*-dimethyl-*para*-bromoaniline radical cations suggested that they might be observable using electrochemical ESR, so experiments were conducted accordingly.

In situ electrolysis of a 2 mM solution of *N,N*-dimethyl-*para*-bromoaniline at a potential of 1.3 V versus Ag using the tubular flow cell yielded a relatively strong ESR signal, with the

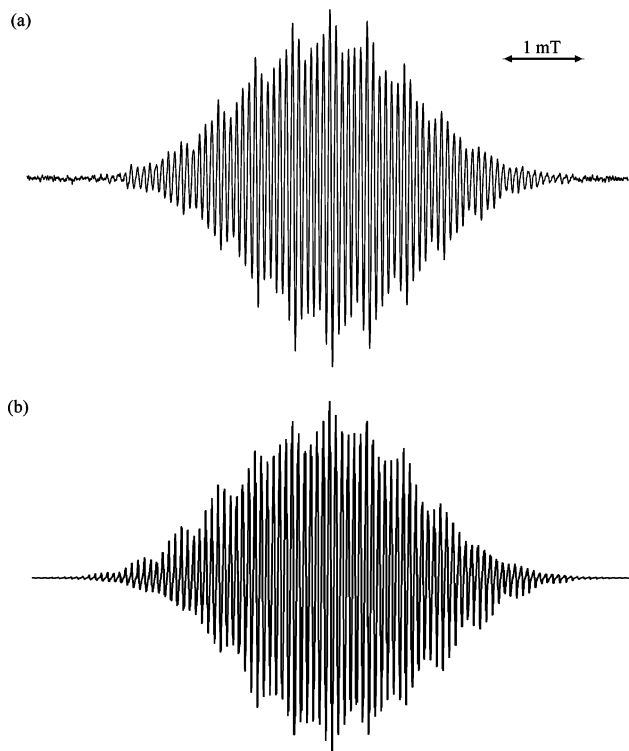
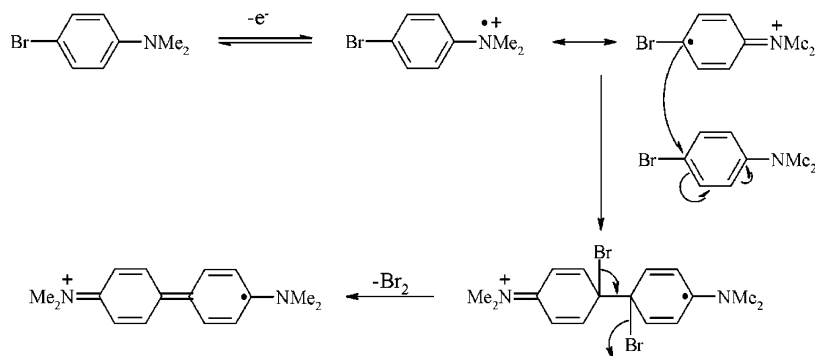


Figure 14. (a) Experimental ESR spectrum obtained from a 2 mM solution of *N,N*-dimethyl-*para*-bromoaniline, flowing at $0.1 \times 10^{-3} \text{ cm}^3 \text{ s}^{-1}$ and potentiostated at 1.3 V vs Ag using a modulation width of 0.02 mT (8×4 min acquisitions). (b) Simulated spectrum using documented hyperfine coupling constants for the radical cation of *N,N,N',N'*-tetramethylbenzidine⁵² and a line width of 0.01 mT.

hyperfine structure shown in Figure 14a. As with the nonmethylated *para*-haloanilines, attempts to simulate the experimental spectrum of the primary radical cation were unsuccessful, but using the hyperfine coupling constants measured for the *N,N,N',N'*-tetramethylbenzidine radical cation,^{52,53} the spectrum in Figure 14b was simulated, which demonstrates excellent agreement with the measured spectrum. This is consistent with a report by Latta and Taft who also observed the *N,N,N',N'*-tetramethylbenzidine radical cation upon bulk electrolysis of *N,N*-dimethyl-*para*-bromoaniline at a platinum gauze.³⁸ Experiments at various flow rates in the range 0.1×10^{-3} to $200 \times 10^{-3} \text{ cm}^3 \text{ s}^{-1}$ revealed that, at steady state, the current normalized signal, S/i_{lim} , was proportional to $V_f^{-2/3}$, with a slope close to $-2/3$, suggesting that the dimer radical cation detected is stable, at least over a period of several minutes.^{25,26} The stability of this dimer radical cation as compared to that generated through the oxidation of *para*-bromoaniline is likely a result of steric factors imposed by the presence of the methyl groups.

SCHEME 4



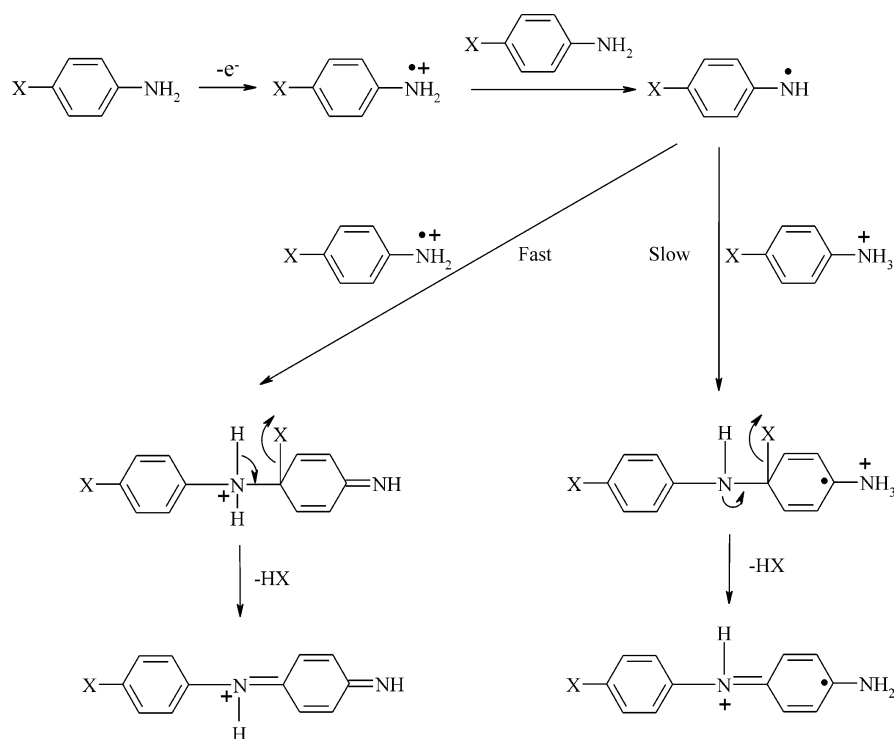
In the work reported by Hand et. al., a mechanism was proposed in which the electrogenerated *N,N*-dimethyl-*para*-haloaniline radical cation ejects a halogen atom to yield a carbene intermediate, two of which combine to give the *N,N,N',N'*-tetramethylbenzidine dication.⁵¹ An alternative mechanism, which rationalizes the ESR spectra observed, is depicted in Scheme 4, where the *N,N*-dimethyl-*para*-bromoaniline radical cation couples tail to tail with a parent *N,N*-dimethyl-*para*-bromoaniline molecule to give a dimer radical cation, which loses molecular bromine, generating the *N,N,N',N'*-tetramethylbenzidine radical cation. In terms of the recorded cyclic voltammetry, this dimer radical cation can be reduced by a single electron on the reverse sweep to give *N,N,N',N'*-tetramethylbenzidine, and the molecular bromine can be reduced to bromide. Schemes 2 and 4 appear quite similar in the fact that the electrogenerated radicals react with parent molecules to yield paramagnetic products, but major differences arise, first in the lack of a deprotonation step for the *N*-methylated aniline and second in the coupling position (i.e., head to tail vs tail to tail), as a result of the blocking of the amino group in the *N*-methylated case.

5. Conclusions

A mechanistic investigation on the voltammetric oxidation of *para*-haloanilines has been reported, and we can conclude that no single reaction mechanism alone can account for the experimental observations. It is evident that, under the experimental conditions employed, the electrogenerated haloaniline radical cation is deprotonated by the parent species to yield a neutral radical which can react with either the parent aniline or another haloaniline radical cation (see Scheme 5). The former process results in the generation of a dimer radical cation which can be detected by ESR, but this reaction is very slow such that no appreciable effects are observed in either the quiescent or hydrodynamic voltammetry. The latter reaction occurs much more quickly, probably since it involves the coming together of two unstable species, rather than one stable and one unstable molecule, to yield the same dimer, but in a higher, non-paramagnetic oxidation state. This dimerization process dominates the voltammetry in that the fast ejection of a hydrogen halide molecule leads to additional anodic currents. The above study has therefore offered a useful insight into the use of electrochemistry and ESR to study different features of the same anodic process, probing mechanistic aspects which may otherwise be overlooked.

Acknowledgment. The authors wish to thank the EPSRC for funding, and A.J.W. thanks JEOL for further financial aid.

SCHEME 5



Appendix A

Newton's Method. The discretized equations given in section 2.4 are nonlinear and therefore must be solved simultaneously using an iterative method. Newton's method is used to solve a system of equations in the form $F(y) = 0$. The matrix form is $y^{z+1} = y^z - [J(y^z)]^{-1} F(y^z)$, where J is the Jacobian matrix found by differentiating each equation in the vector F with respect to each term in y that appears in the equation:

$$J(y) = \begin{bmatrix} \frac{\partial f_1}{\partial y_1} & \frac{\partial f_1}{\partial y_2} & \dots & \frac{\partial f_1}{\partial y_n} \\ \frac{\partial f_2}{\partial y_1} & \frac{\partial f_2}{\partial y_2} & \dots & \frac{\partial f_2}{\partial y_n} \\ \vdots & \vdots & \ddots & \vdots \\ \frac{\partial f_n}{\partial y_1} & \frac{\partial f_n}{\partial y_2} & \dots & \frac{\partial f_n}{\partial y_n} \end{bmatrix}$$

Introduction of the vector u where $u = y^{z+1} - y^z$ yields the system of equations

$$Ju = -F$$

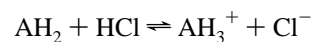
which may be solved by a standard linear method. The process is iterated until the termination criterion is met, when $\sqrt{(y^{z+1} - y^z)^2} < \epsilon$.

Appendix B

UV–Visible Spectroscopy. A solution of HCl was prepared by bubbling anhydrous hydrogen chloride (5% in helium) through a flask containing 50 mL of acetonitrile for 30 min. This saturated solution was then diluted 1:20 with more acetonitrile. Initially, it was necessary to estimate the concentration of HCl in the solution, since there is very little literature

surrounding the solubility of HCl in acetonitrile. This was achieved by carrying out a UV–visible titration using the base 2,6-lutidine. The UV spectrum of 0.2 mM 2,6-lutidine in acetonitrile was recorded, where an absorption band in the region of 266 nm was observed, in good agreement with documented spectra for 2,6-lutidine in water.⁴⁶ Upon the addition of aliquots of the above prepared HCl solution, the band gradually shifted to 270 nm, with an increase in absorbance, as shown in Figure 15a. This variation is consistent with the aqueous phase spectra observed by Andon and co-workers⁴⁶ for 2,6-lutidine under conditions of strong acid and alkali, the change being attributed to the protonation of lutidine at low pH. It can be seen from Figure 15a that after the addition of 90 μ L of the HCl solution, further addition of HCl has no further effect on the spectrum, suggesting an “end point” in the titration of the base with HCl, where all of the lutidine has been protonated. If we assume a 1:1 stoichiometry, we can conclude that 90 μ L of the HCl solution contains the same number of moles as 3 mL of 0.2 mM lutidine (6×10^{-7} mol), suggesting a concentration of 6.67 mM. Interestingly, if we assume that the saturated solution of HCl from which the above solution was made was 20 times as concentrated, then we can estimate the solubility of HCl in acetonitrile as 133 mM at 298 K.

Once the HCl solution concentration had been established, the same methodology as above was used to investigate the following equilibrium:



The UV spectrum of 0.1 mM *para*-chloroaniline was recorded, in which an absorption band at 248 nm was observed which decreased in intensity upon the addition of HCl solution, as shown in Figure 15b. After the addition of approximately 40 mM HCl, the absorption intensity reached a minimum such that further additions had no effect on the spectrum, suggesting that the absorbance gives a measure of the neutral AH_2 concentration,

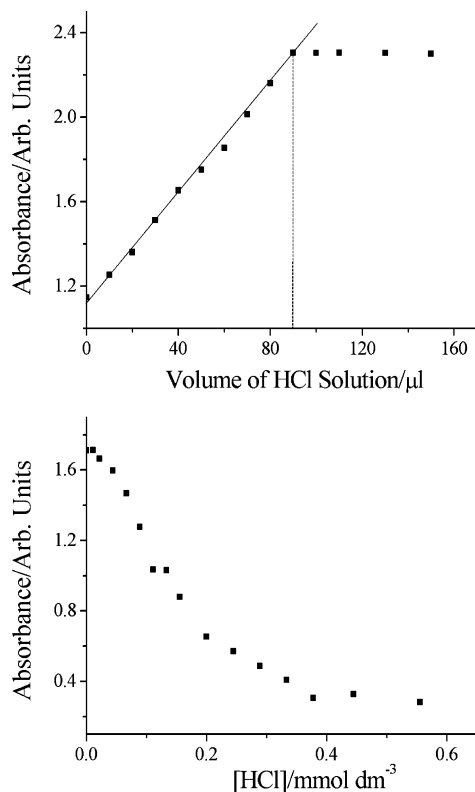


Figure 15. (a) UV absorption at 270 nm as a function of added HCl solution to a 3 mL volume of 0.2 mM 2,6-lutidine in acetonitrile. (b) UV absorption at 248 nm of a solution of 0.1 mM *para*-chloroaniline as a function of HCl concentration.

allowing us to calculate the equilibrium constant, defined as

$$K_{\text{eq}} = \frac{[\text{AH}_3^+][\text{Cl}^-]}{[\text{AH}_2][\text{HCl}]}$$

For a given total concentration of HCl, the value of $[\text{AH}_3^+]$ and therefore $[\text{Cl}^-]$ can be determined from the decrease in absorbance as a fraction of the maximum absorbance (i.e., that in the absence of any HCl). Using the data in Figure 15b, at HCl concentrations of 0.050 and 0.025 mM, K_{eq} was calculated at 0.012 and 0.004, respectively. These concentrations were chosen, since during the electrolysis of *para*-chloroaniline one chloride anion is ejected for every two parent molecules, and thus, the chloride concentration can never be more than half that of the *para*-chloroaniline (at a concentration of 0.1 mM in this experiment). Although there is a large degree of error in these values (0.008 ± 0.004), these experiments serve to establish the fact that, under the reaction conditions employed, HCl is not significantly dissociated.

References and Notes

- Geniès, E. M.; Boyle, A.; Lapkowski, M.; Tsintavis, C. *Synth. Met.* **1990**, *36*, 139.
- Syed, A. A.; Dinesan, M. K. *Talanta* **1991**, *38*, 815.
- Wawzonek, S.; McIntyre, T. W. *J. Electrochem. Soc.* **1967**, *114*, 1025.
- Wawzonek, S.; McIntyre, T. W. *J. Electrochem. Soc.* **1972**, *119*, 1350.
- Mohilner, D. M.; Adams, R. N.; Argersinger, W. J. *J. Am. Chem. Soc.* **1962**, *84*, 3618.
- Mu, S.; Chen, C.; Wang, J. *Synth. Met.* **1997**, *88*, 249.
- Karyakin, A. A.; Vuki, M.; Lukachova, L. V.; Karyakina, E. E.; Orlov, A. V.; Karpachova, G. P.; Wang, J. *Anal. Chim. Acta* **1999**, *452*, 1.
- Zhang, X.; Ogorevc, B.; Wang, J. *Anal. Chim. Acta* **2002**, *452*, 1.
- Saber, T. M. H.; Farsang, G.; Ladányi, L. *Microchem. J.* **1972**, *17*, 220.
- Speiser, B.; Rieker, A. *J. Electroanal. Chem.* **1983**, *147*, 205.
- Pekmez, N.; Pekmez, K.; Yildiz, A. *J. Electroanal. Chem.* **1993**, *348*, 389.
- Nelson, R. F.; Adams, R. N. *J. Am. Chem. Soc.* **1968**, *90*, 3925.
- Bacon, J.; Adams, R. N. *J. Am. Chem. Soc.* **1968**, *90*, 6596.
- Amatore, C.; Farsang, G.; Maisonnaire, E.; Simon, P. *J. Electroanal. Chem.* **1999**, *462*, 55.
- Kádár, M.; Takáts, Z.; Karancsi, T.; Farsang, G. *Electroanalysis* **1999**, *11*, 809.
- Kádár, M.; Nagy, Z.; Karancsi, T.; Farsang, G. *Electrochim. Acta* **2001**, *46*, 1297.
- Kádár, M.; Nagy, Z.; Karancsi, T.; Farsang, G. *Electrochim. Acta* **2001**, *46*, 3405.
- Pusztai, S.; Dankházi, T.; Farsang, G. *Electroanalysis* **2003**, *15*, 539.
- Pusztai, S.; Pánczél, J.; Dankházi, T.; Farsang, G. *J. Electroanal. Chem.* **2004**, *571*, 233.
- Petr, A.; Dunsch, L. *J. Phys. Chem.* **1996**, *100*, 4867.
- Goldberg, I. B.; Bard, A. J. *J. Phys. Chem.* **1974**, *78*, 290.
- Goldberg, I. B.; Boyd, D.; Hirasawa, R.; Bard, A. J. *J. Phys. Chem.* **1974**, *78*, 295.
- Rapta, P.; Kress, L.; Hapiot, P.; Dunsch, L. *Phys. Chem. Chem. Phys.* **2002**, *4*, 4181.
- Wadhawan, J. D.; Compton, R. G. In *Encyclopedia of Electrochemistry*; Bard, A. J., Stratmann, M., Eds.; Wiley-VCH Verlag GmbH and Co.: Weinheim, Germany, 2003; Vol. 2, Chapter 3.
- Albery, W. J.; Compton, R. G.; Kerr, I. S. *J. Chem. Soc., Perkin Trans. 2* **1981**, 825.
- Wain, A. J.; Thompson, M.; Klymenko, O. V.; Compton, R. G. *Phys. Chem. Chem. Phys.* **2004**, *6*, 4018.
- Coles, B. A.; Compton, R. G. *J. Electroanal. Chem.* **1981**, *127*, 37.
- Albery, W. J.; Chadwick, A. T.; Coles, B. A.; Hampson, N. A. *J. Electroanal. Chem.* **1977**, *75*, 229.
- Blaedel, W. J.; Klatt, L. N. *Anal. Chem.* **1966**, *38*, 879.
- Blaedel, W. J.; Olson, C. L.; Sharma, L. R. *Anal. Chem.* **1963**, *35*, 2100.
- Levich, V. G. *Physicochemical hydrodynamics*; Prentice-Hall: 1962.
- Thompson, M.; Klymenko, O. V.; Compton, R. G. *J. Electroanal. Chem.*, in press.
- Alden, A. J.; Compton, R. G. *J. Electroanal. Chem.* **1996**, *404*, 27.
- Albery, W. J.; Compton, R. G.; Chadwick, A. T.; Coles, B. A.; Lenkait, J. A. *J. Chem. Soc., Faraday Trans. 1* **1980**, *76*, 1391.
- Arfken, G. B.; Weber, H. J. *Mathematical Methods for Physicists*; Harcourt: 2001.
- Weil, J. A.; Bolton, J. R.; Wertz, J. E. *Electron Paramagnetic Resonance, Elementary Theory and Practical Applications*; John Wiley and Sons: 1994.
- Liu, Y.; Xu, G.; Sha, J.; Guo, J.; Tang, Y. *Acta Chem. Sin.* **1988**, *4*, 365.
- Latta, B. M.; Taft, R. W. *J. Am. Chem. Soc.* **1967**, *89*, 5172.
- Seo, E. T.; Nelson, R. F.; Fritsch, J. M.; Marcoux, L. S.; Leedy, D. W.; Adams, R. N. *J. Am. Chem. Soc.* **1966**, *88*, 3498.
- Male, R.; Allendoerfer, R. D. *J. Phys. Chem.* **1988**, *92*, 6237.
- Petr, A.; Dunsch, L. *J. Electroanal. Chem.* **1996**, *419*, 55.
- Janz, G. J.; Danyluk, S. S. *J. Am. Chem. Soc.* **1959**, *81*, 3846.
- Coetzee, J. F.; Kolthoff, I. M. *J. Am. Chem. Soc.* **1957**, *79*, 6110.
- Hall, H. K. *J. Am. Chem. Soc.* **1956**, *63*, 63.
- Kolthoff, I. M.; Bruckenstein, S.; Chantooni, M. K. *J. Am. Chem. Soc.* **1961**, *83*, 3927.
- Andon, R. J. L.; Cox, J. D.; Herington, E. F. G. *Trans. Faraday Soc.* **1954**, *50*, 918.
- Gross, K. C.; Seybold, P. G. *J. Org. Chem.* **2001**, *66*, 6919.
- Iweibo, I.; Oderinde, R. A.; Faniran, J. A. *Spectrochim. Acta* **1982**, *38A*, 1.
- Wilke, C. R.; Chang, P. *Am. Inst. Chem. Eng. J.* **1955**, *1*, 264.
- Timofeeva, Z. N.; Kudryavtseva, T. K. *Elektrokhimiya* **1977**, *13*, 1387.
- Hand, R.; Melicharek, M.; Scoggin, D. I.; Stotz, R.; Carpenter, A. K.; Nelson, R. F. *Collect. Czech. Chem. Commun.* **1971**, *36*, 842.
- Smejtek, P.; Honzl, J.; Metalová, V. *Collect. Czech. Chem. Commun.* **1965**, *30*, 3875.
- Fritsch, J. M.; Adams, R. N. *J. Chem. Phys.* **1965**, *43*, 1887.